Rapid discovery of antiviral targets through dimensionality reduction of genome-scale metabolic models

Yong-ki Lee[1,2,3#], Seongmo Kang[2#], JinA Lim[2#], Kanghee Kim[1,4], Se-Mi Kim[1], Mark Anthony B. Casel[1], Issac Choi[1], Young Ki Choi[1,4*], Hyun Uk Kim[2,5,6*], and Yoosik Kim[2,3,5,7*]

[1]Center for Study of Emerging and Re-emerging Viruses, Korea Virus Research Institute, Institute for Basic Science (IBS), Daejeon 34126, Republic of Korea
[2]Department of Chemical and Biomolecular Engineering, Korea Advanced Institute of Science and Technology (KAIST), Daejeon 34141, Republic of Korea
[3]KAIST Institute for Health Science and Technology, KAIST, Daejeon 34141, Republic of Korea
[4]College of Medicine and Medical Research Institute, Chungbuk National University, Cheongju 28644, Republic of Korea
[5]Graduate School of Engineering Biology, KAIST, Daejeon 34141, Republic of Korea
[6]BioProcess Engineering Research Center and BioInformatics Research Center, KAIST, Daejeon 34141, Republic of Korea
[7]KAIST Institute for BioCentury, KAIST, Daejeon 34141, Republic of Korea

[#]These authors contributed equally to this work
*Correspondence: Young Ki Choi (choiki55@ibs.re.kr), Hyun Uk Kim (ehukim@kaist.ac.kr), and Yoosik Kim (ysyoosik@kaist.ac.kr)

ABSTRACT
The COVID-19 pandemic underscored the urgent need for rapid and broadly applicable strategies to identify antiviral targets against emerging pathogens. Conventional approaches, which rely on detailed viral characterization and large-scale drug screening, remain too slow to address this challenge. Here, we introduce a transcriptome-based computational framework that integrates genome-scale metabolic models with dimensionality reduction to uncover host metabolic vulnerabilities that support viral replication. Applying this approach to bulk and single-cell RNA-seq data from HCoV-OC43–infected cells and organoids identified oxidative phosphorylation as a key vulnerability, and pharmacological inhibition of complex I effectively curtailed viral replication. Extending the framework to SARS-CoV-2 and MERS-CoV revealed pyrimidine catabolism as a conserved antiviral pathway, with inhibition of its rate-limiting enzyme DPYD suppressing replication in organoid models. Re-analysis of patient metabolome data further confirmed elevated DPYD activity during COVID-19, underscoring its clinical relevance. Together, these findings establish a generalizable and rapid strategy for host-directed antiviral discovery, providing a foundation for precision therapeutics and pandemic preparedness.

INTRODUCTION

The COVID-19 pandemic has sparked broad interest in developing antiviral strategies to combat emerging and recurring viral threats. Extensive research into the replication mechanisms of the SARS-CoV-2 virus has facilitated both the discovery of novel antiviral drugs and repurposing efforts, exemplified by Nirmatrelvir and Molnupiravir, respectively. In conjunction with mRNA vaccines, these therapeutic interventions have played a pivotal role in shifting the pandemic to its current endemic phase. However, this transition has come at the cost of substantial human loss and profound social and economic disruption, highlighting the need for more efficient and rapid response systems. In this context, antiviral research is expanding into perspectives, one of which focuses on modifying host metabolism to hinder viral replication.

In infected cells, viruses alter the host cells' metabolism to facilitate their reproduction (*1, 2*). In particular, glucose and fatty acid metabolism have been identified as critical regulatory pathways to support replication of numerous viruses (*3*). Furthermore, a broad range of host metabolic pathways has been reported to be altered in response to viral infection (*4, 5*). Inspired by these findings, several studies modulated specific metabolic pathways, including those related to pyrimidine (*6, 7*), glutamine (*8*), lipid (*9*), and fatty acid (*10, 11*) synthesis, to inhibit viral replication. Others have focused on the role of individual metabolites, showing that specific metabolites can influence viral infectivity and pathogenesis (*12, 13*). However, pinpointing target pathways requires iterative screening experiments and insight into virus-host interactions, thereby posing challenges for prompt response against emerging viruses.

To address this limitation, *in silico* approaches, such as virtual screening, have been explored (*14, 15*). Of these, the genome-scale metabolic model (GEM) stands out as a powerful tool for deciphering complex metabolic networks of organisms through genome-protein-reaction (GPR) associations (*16, 17*). Multi-omics databases from various biological samples can be integrated to generate context-specific GEMs (*18*), which can be used to analyze the metabolic flux profiles and predict the effects of a single-gene inhibition on the overall metabolic flux (*19*). More importantly, these models can be used to identify biomarkers or discover therapeutic targets (*20-22*). In the context of viral infection, GEM can be employed to understand the infection-triggered alterations in metabolic pathways and to identify enzymes utilized by the viruses to support their replication (*23-27*). Nevertheless, these studies have primarily focused on reducing viral biomass or on specific metabolic pathways showing increased flux in infected hosts, with less emphasis on the global metabolic changes induced by viruses.

Here, we introduce a computational framework that GEMs with Uniform Manifold Approximation and Projection (UMAP) to capture the metabolic state of virus-infected cells and pinpoint host enzymes whose inhibition reverts the infected metabolic profile toward that of uninfected cells, thereby suppressing viral replication (Figure 1). We first validated this approach using publicly available RNA-seq datasets from HCoV-OC43- and HCoV-229E-infected cells, confirming its ability to identify relevant metabolic perturbations. We next extended the analysis to single-cell RNA-seq (scRNA-seq) profiles generated from human bronchial epithelial (HBE) organoids infected with HCoV-OC43, demonstrating its applicability in complex tissue models. Finally, we applied the framework to two high-priority coronaviruses lacking effective treatments, SARS-CoV-2 and MERS-CoV, uncovering conserved metabolic vulnerabilities. Collectively, this strategy provides a generalizable, transcriptome-based platform to dissect virus–host metabolic interactions and rapidly nominate antiviral targets without the need for prior viral characterization or chemical screening.

RESULTS

Antiviral Target Discovery via Metabolic Alterations

We first utilized publicly available RNA-seq data to demonstrate the feasibility of the proposed approach for discovering antiviral targets through metabolic alteration. We generated infection-specific GEMs using datasets from two cell lines infected with common human coronaviruses (HCoVs) (MRC-5 lung fibroblast cells infected with HCoV-229E and A549-ACE2 lung adenocarcinoma cells infected with HCoV-OC43) (Figure 2A). Each infection-specific GEM comprises a "control GEM" reconstructed from pre-infection (uninfected) data and an "infected GEM" from post-infection (infected) data. The Human1 model (*28*) served as a reference template for human metabolism when generating GEMs. We then inferred the metabolic flux profiles of entire GEMs using the least absolute deviation (LAD) and subsequently employed the UMAP dimensionality reduction algorithm to simplify the complexity of those flux profiles. The UMAP visualization represents individual samples as points, with each point encompassing the entire metabolic flux profile of the sample. We found that both RNA-seq data exhibited distinct clustering between the flux profiles of control and infected cells (Figure 2B, highlighted in blue and red boxes). These results indicate that viral infection causes significant metabolic changes in host cells, enabling the identification of potential targets to revert the cells to their uninfected state.

We then performed single-gene knockout simulations on the GEMs of infected cells to investigate the metabolic flux differences induced by gene perturbations. Our analysis revealed several single-gene knockout simulated flux profiles that were clustered with that of the uninfected sample (Figure 2B, magnified blue boxes). We considered these genes as potential antiviral targets, as their deletion is predicted to shift the overall metabolic flux of infected cells toward one resembling that of uninfected cells. Indeed, we have previously experimentally validated that this approach can successfully impact overall metabolism and influence the cellular response to chemotherapy drugs in breast cancer cells, serving as a model system (*29*).

A detailed investigation of these profiles revealed that genes in this cluster were functionally related. The subsystem of target genes in HCoV-229E was predominantly associated with porphyrin metabolism (Table S1A), while those in HCoV-OC43 were related to oxidative phosphorylation (OXPHOS) (Table S1B). Comparison of GEMs between control and infected cells confirmed that the target reaction flux was elevated following viral infection (Figure 2C). Of note, increased flux is not the primary criterion for target selection in our framework. Yet, many of the candidate genes show increased flux upon infection, suggesting that they may play an important role in metabolic alterations during infection. Moreover, gene ontology (GO) and gene set enrichment analysis (GSEA) of the RNA-seq data did not show porphyrin metabolism and oxidative phosphorylation as significantly upregulated pathways (Figure S1). Based on these findings, we proceeded to investigate the potential impact of metabolic pathways derived from the framework on viral infection.

Porphyrin is a heterocyclic ring compound composed of four pyrrole subunits connected by methine bridges, serving as a framework for heme synthesis. Since no small molecule inhibitors targeting porphyrin metabolism have been discovered to date, short-hairpin RNA (shRNA) was utilized as an alternative approach. We selected aminolevulinate dehydratase (*ALAD*) and solute carrier family 25 member 38 (*SLC25A38*), which are involved in the initial process of porphyrin biosynthesis (*30*), as knockdown targets among the seven candidate genes (Figure 2D). To mimic a single-gene knockout simulation, MRC-5 cells were transduced with lentiviral vectors encoding shALAD or shSLC25A38 RNAs (hereafter referred to as shALAD and shSLC25A38 cells, respectively). Comparison of their gene expression levels with those of shScramble cells confirmed efficient knockdown (Figure S2A). The impact of target suppression on HCoV-229E replication was evaluated by infecting shScramble, shALAD, and shSLC25A38 cells with HCoV-229E under the same conditions as

dataset GSE155986. To account for potential shRNA-related effects, the experiments were repeated in MRC-5 wild-type (WT) cells. A comparative analysis of intracellular viral gene levels revealed a significant reduction in viral gene expression in shALAD and shSLC25A38 cells, whereas no substantial differences were detected between MRC-5 WT and shScramble cells (Figure 2E). The measurement of extracellular viral load from cell supernatants also showed no significant difference between MRC-5 WT and shScramble samples. In contrast, a decreased viral titer was observed in shALAD and shSLC25A38 cells, with a more pronounced log reduction (2.33) in the shSLC25A38 sample (Figure 2F).

The anti-HCoV-OC43 target genes identified through our framework were strongly associated with OXPHOS, specifically the subunit of complex IV (cytochrome c oxidase, CIV). CIV facilitates the transfer of electrons via cytochrome c to generate the proton gradient essential for ATP synthesis and cellular respiration (Figure 2G). We found that ADDA 5 and chlorpromazine (CPZ) are highly selective inhibitors of CIV (*31, 32*). Although CPZ is an FDA-approved psychotropic drug, its antiviral properties have already been demonstrated (*33, 34*) through the inhibition of clathrin-mediated endocytosis (*35*), a key mechanism of viral entry. Given the limited studies on ADDA 5 in the context of viral infections, we decided to investigate its potential antiviral effects against HCoV-OC43. A dose-response curve in A549-ACE2 cells revealed a 50% cytotoxic concentration (CC_{50}) of 33 μM for ADDA 5 (Figure 4H, blue). Hence, we applied 20 μM (~75% cell viability) to A549-ACE2 cells as a post-treatment following HCoV-OC43 infection. Notably, this treatment did not impair the viability of infected cells (Figure 4H, red), but it led to a significant reduction in intracellular viral gene expression at 48 hours post-infection (hpi) (Figure 2I). The plaque assay further demonstrated a 2.2 log reduction (99.4%) in extracellular viral load following ADDA 5 treatment (Figure 2J and Figure S2B), providing experimental evidence that CIV inhibition effectively blocks HCoV-OC43 replication. Taken together, our results confirm that the proposed anti-HCoV targets identified by our framework can indeed modulate virus replication.

Application of the Framework for HCoV-OC43-infected Human Organoids

Organoids more accurately recapitulate tissue architecture and intercellular interactions than conventional monolayer cultures. Recent advances in organoid technology and transcriptomic profiling have enabled detailed characterization of host responses across diverse cell types during viral infection (*36, 37*). In particular, respiratory organoids differentiated under air–liquid interface (ALI) conditions reproduce cellular exposure to air and serve as robust models for studying airborne pathogens (*38, 39*). However, the complexity and high dimensionality of scRNA-seq data make it challenging to systematically identify antiviral host factors. To address this limitation, we applied our computational framework to scRNA-seq data and evaluated its ability to identify reliable antiviral targets. We used our previously published dataset GSE262439 (*39*), which profiled human bronchial epithelial (HBE) organoids infected with four beta-coronaviruses (HCoV-OC43, SARS-CoV-2, MERS-CoV, and SARS-CoV) (Figure 3A).

To construct GEMs from scRNA-seq data, we first assessed the suitability of a bootstrapping strategy using the down-sampling-based variation estimation (DSAVE) method (*40*) (Figure 3B). This analysis revealed that minimizing sample bias to levels comparable with bulk data required pooling more than half of the cells per sample, rendering bootstrapping infeasible (Figure S3). Therefore, we reconstructed infection-specific GEMs at a pseudo-bulk scale using all cells from each sample. Although the total cell number varied (2,781–5,727 cells), normalized read counts were comparable across samples, except for the SARS-CoV–infected organoids, which were excluded from further analysis (Figure 3C).

As in the cell-line models, we performed single-gene knockout simulations on the organoid GEMs and analyzed metabolic flux profiles from control, infected, and knockout-

simulated conditions using UMAP. This analysis again revealed antiviral targets capable of shifting infected metabolic states toward those of uninfected cells (Figure 3D). Notably, the oxidative phosphorylation (OXPHOS) subsystem emerged as a vulnerability in HCoV-OC43–infected organoids, consistent with our findings in monolayer cultures (Figure 2B). In organoids, however, the predicted targets encompassed 44 subunits of OXPHOS complex I (Table S2A).

Complex I (NADH–ubiquinone oxidoreductase, CI) initiates the respiratory chain by oxidizing NADH and transferring electrons to ubiquinone (Figure 3E). Among known CI inhibitors, rotenone is primarily used as an insecticide, while the FDA-approved type II diabetes drug metformin has been reported to exert broad-spectrum antiviral activity (*41*). We therefore selected IACS-010759, a selective CI inhibitor without prior application in antiviral studies, for experimental validation. HBE organoids were infected with HCoV-OC43 via the apical side, and IACS-010759 was added daily to the basolateral compartment under ALI conditions (Figure 3F). Consistent with computational predictions, treatment with IACS-010759 led to a dose-dependent reduction in viral gene expression (Figure 3G and S4A) and viral RNA copy number in the supernatant (Figure 3H and S4B). At 100 nM, both intracellular and extracellular viral RNA levels decreased, although mild cytotoxicity (<75% viability) was observed (Figure S4C). To further confirm specificity, we tested IACS-010759 in Vero E6 cells, a standard model for coronavirus research. The drug exhibited potent antiviral activity at non-cytotoxic concentrations (<0.5 μM) (Figure 3I), yielding a high selectivity index (CC_{50}/EC_{50}) against HCoV-OC43. Together, these results validate OXPHOS complex I inhibition as an effective antiviral strategy identified by our framework, demonstrating that computationally derived targets can translate into experimentally verifiable therapeutic vulnerabilities.

Framework Extension Reveals a Conserved Antiviral Target in SARS-CoV-2 and MERS-CoV

Encouraged by the successful validation in HCoV-OC43–infected organoids, we next applied our framework to two high-priority coronaviruses lacking effective treatments: SARS-CoV-2 and MERS-CoV. Computational analysis of infected samples consistently identified genes associated with pyrimidine catabolism as candidate antiviral targets (Figure 4A–B and Table S3A–B). Although annotated under both pyrimidine metabolism and β-alanine metabolism subsystems in Human1, the identified reactions converge on the pyrimidine catabolic pathway, hereafter referred to as "pyrimidine catabolism." This pathway comprises a three-step enzymatic process converting uracil and thymine into β-alanine and D-3-aminoisobutanoate, respectively. The first and rate-limiting step is catalyzed by dihydropyrimidine dehydrogenase (DPYD), which reduces pyrimidines to dihydropyrimidines (Figure 4C). Notably, DPYD has not been previously studied in the context of viral infection, prompting us to examine its potential as a therapeutic target using the inhibitor Eniluracil.

We first evaluated the cytotoxicity of Eniluracil in A549-ACE2 and Vero E6 cells (Figure 4D). Both cell types tolerated concentrations up to 50 μM without notable cytotoxicity, while mild toxicity was observed at 100 μM. In A549-ACE2 cells, a significant reduction in viral RNA copy number was detected only at 100 μM (Figure S5A). Nevertheless, viral titers decreased substantially at 50 μM, with reductions of 87.0% for SARS-CoV-2 and 78.5% for MERS-CoV (Figure 4E). In Vero E6 cells, Eniluracil treatment at 50 μM robustly inhibited replication of both viruses (92.3% for SARS-CoV-2 and 95.4% for MERS-CoV), and notably, MERS-CoV replication was suppressed by >90% even at 10 μM, corresponding to a favorable selectivity index (>10) (Figure 4E). Reductions in viral RNA copy numbers further corroborated these results (Figure S5B). Together, these findings establish pyrimidine catabolism, specifically DPYD inhibition, as a previously unrecognized vulnerability in SARS-

CoV-2 and MERS-CoV, extending the applicability of our framework to uncover novel, host-directed antiviral strategies.

Validation of DPYD as an Antiviral Target in Organoids and Patient Metabolomes

To evaluate whether the antiviral activity of DPYD inhibition extends beyond cell lines to more physiologically relevant systems, we tested Eniluracil in HBE organoids infected with SARS-CoV-2 or MERS-CoV. In organoids, Eniluracil treatment showed no detectable cytotoxicity even at 100 μM (Figure S6A). Given that drug penetration may be reduced in three-dimensional structures, we modified the treatment scheme by directly delivering Eniluracil to the apical side in addition to the basolateral compartment (*42*) (Figure 5A). Under these conditions, immunohistochemistry (IHC) revealed a pronounced reduction of viral nucleocapsid protein levels in Eniluracil-treated organoids, indicating suppressed replication (Figure 5B–C). Consistently, viral titers and RNA copy numbers in the supernatant were significantly decreased (Figure 5D and S6B), confirming the antiviral efficacy of Eniluracil against both SARS-CoV-2 and MERS-CoV in the organoid model. Importantly, gene expression profiles and pathway enrichment analyses from scRNA-seq data showed no significant alterations in OXPHOS or pyrimidine catabolism pathways (Figure S7A–E), underscoring that our computational framework uncovered therapeutic vulnerabilities not apparent through conventional transcriptomic analysis alone.

To further assess the clinical relevance of targeting DPYD, we examined its enzymatic activity in COVID-19 patients. DPYD activity was estimated using the metabolite ratio of dihydropyrimidine to pyrimidine (*43, 44*). Re-analysis of a publicly available plasma metabolome dataset (*45*) revealed a significant increase in the dihydrothymine-to-thymine ([DHT]/[THY]) ratio in COVID-19 patients (n = 104) compared with healthy controls (n = 62) (Figure 5E). These findings indicate enhanced DPYD activity during SARS-CoV-2 infection, supporting its potential as a clinically relevant antiviral target.

DISCUSSION

In this study, we developed a computational framework that combines GEM with UMAP for rapid discovery of antiviral targets. Our framework focuses on "metabolic rewiring," restoring virus-altered metabolic pathways to a state that most closely resembles the pre-infected condition by employing single-gene knockout simulations. To achieve this, we meticulously constructed infection-specific GEMs based on transcriptomics data and incorporated UMAP-based dimensionality reduction to effectively identify key target genes among the various metabolic pathways altered during viral infection.

When we applied our framework to MRC-5 cells infected with HCoV-229E and A549-ACE2 cells infected with HCoV-OC43, genes associated with the porphyrin metabolism and OXPHOS subsystem (complex IV) emerged as antiviral targets, respectively. The antiviral effect of inhibiting these pathways was demonstrated using shRNAs and small chemical inhibitors. These key metabolic pathways cannot be discovered under conventional analysis of RNA-seq data, such as differential gene expression or pathway enrichment analyses. It is worth noting that OXPHOS complex V (reaction MAR06916) also showed a marked flux increase in HCoV-OC43-infected cells (Figure 2C), but it was not predicted to be the target. This is because our framework does not prioritize magnitude of changes in specific metabolic flux. Instead, by leveraging GPR associations, it focuses on gene-level regulators that can drive optimal rewiring of the host's whole metabolic network.

Our framework remained effective in identifying antiviral targets even when applied to highly complex scRNA-seq datasets. From HBE organoids infected with beta-CoVs, we again confirmed the OXPHOS subsystem (complex I) as an antiviral target for HCoV-OC43, and identified the pyrimidine catabolism for both SARS-CoV-2 and MERS-CoV. To the best of our knowledge, this is the first study to establish a link between these metabolic processes and viral infection, underscoring the originality of our framework in providing perspectives without prior knowledge of the virus.

Additionally, our framework highlights genes encoding solute carrier proteins (SLC) involved in transport reactions as potential antiviral targets. The SLC family comprises ~450 membrane transporters that mediate the exchange of diverse substrates, including amino acids, inorganic ions, and metabolites (*46, 47*). Several members of this family are already known to be associated with viral infections. For example, the bile salt transporter SLC10A1 (NTCP) is a well-established receptor for hepatitis B virus (*48*), known to form a complex with the preS1 domain of the viral surface protein (*49*). The heterodimeric amino acid transporter SLC3A2 (CD98 heavy chain) has been implicated in the hepatitis C viral entry process (*50*). SLC15A3 and SLC30A1 (ZnT1) have been associated with herpes simplex virus 1 and vesicular stomatitis virus infections, respectively (*51, 52*).

We confirmed that the knockdown of the glycine transporter gene *SLC25A38*, one of the predicted targets for HCoV-229E, effectively reduced viral RNA replication. Moreover, analysis of the HBE organoids scRNA-seq dataset revealed the *SLC32A1*, which mediates extracellular transport of glycine and β-alanine, as a shared candidate target for SARS-CoV-2- and MERS-CoV (Table S3A-B). These findings collectively suggest that certain SLC proteins may serve as key regulators in the host's metabolic remodeling in response to viral infections. Further systematic studies on SLC transporters will pave the way for clarifying their roles in viral replication and exploring their therapeutic potential as antiviral targets.

One limitation of our study is that some of the identified targets may represent key regulators of host metabolism that are closely linked to cell survival. For example, the OXPHOS subsystem identified from HCoV-OC43-infected samples is a central pathway for host energy and redox homeostasis. While targeting this pathway can suppress viral replication, it may also compromise the viability of host cells. Therefore, antiviral strategies that interfere with such essential pathways should be approached with caution, and the trade-off between

antiviral efficacy and host cell viability must be carefully considered. Another limitation of such host-directed therapies (HDTs) is the difficulty in excluding potential off-target effects. Although we utilized selective inhibitors with well-established metabolic functions, they may induce unexpected effects and affect cell signaling pathways by inhibiting off-target enzymes. Nevertheless, HDTs offer several advantages, including a lower risk of resistance, applicability across diverse variants, and feasibility for drug repurposing, making them a promising strategy against future viral threats.

In summary, our computational framework enables the detection of previously overlooked metabolic targets by capturing virus-induced alterations in host metabolism. The experimental validation of these targets underscores the robustness of our approach, suggesting its potential applicability across a broad spectrum of virus-infected samples. We envision the developed framework serving as a strategic foundation for exploring tailored HDTs against emerging and recurrent viruses.

MATERIALS AND METHODS

Infection-specific GEM extraction, flux simulation, and dimensionality reduction

Infection-specific GEMs were constructed for control and infected samples from each input dataset, using the Human1 template (*27*) (version 1.6.0) and rank-based task-driven integrative network inference for tissues (rank-based tINIT) (*53*). Metabolic fluxes for both control and infected samples were calculated using the least absolute deviation (LAD) method (*54*) with a threshold of 0.01 added as a constraint on the biomass formation rate to simulate a more realistic flux (i.e., cell growth rate > 0 for the control sample). For single-gene knockout simulation in the infected model, flux changes were predicted through the linear minimization of metabolic adjustment (lMOMA) (*55*). In this case, constraints were introduced to set the upper and lower bounds of reactions eliminated by single-gene knockout to 0. The reconstruction of all infection-specific GEMs was carried out in MATLAB (R2021a) using Gurobi Optimizer (version 9.1.2). The reading, writing, and manipulation of the COBRA-compliant MATLAB files were implemented using COBRApy (version 0.23.1) (*19*). Dimensionality reduction analysis of total flux sets (control sample, infected sample, and single-gene knockout simulation results) was executed by UMAP (version 0.5.1) (*56*) with optimized parameters (n_neighbors = 3 or 7, min_dist = 0.1). All UMAP plots were visualized using Seaborn (version 0.11.0) and Matplotlib (version 3.3.4) libraries.

RNA-seq data processing

A total of three publicly available RNA-seq datasets were utilized in this study (details summarized in Table S4). To construct infection-specific GEMs, transcripts per million (TPM) values were required. When datasets provided only raw read counts, transcript lengths were retrieved from the Ensembl API (*57*), followed by TPM normalization. Based on raw read counts, differentially expressed genes (DEGs) were identified using the DEGseq package (version 1.14.0) (*58*) for bulk RNA-seq and the DESeq2 (version 1.46.0) (*59*) for scRNA-seq. GO enrichment analysis and GSEA were performed with the clusterProfiler package (version 4.14.3) (*60*). Results were visualized using the ggplot2 (version 3.5.1) and ComplexHeatmap (version 2.22.0) packages (*61*) in R (version 4.4.2).

Viral titration

Human beta-coronavirus strain OC43 (HCoV-OC43) and alpha-coronavirus strain 229E (HCoV-229E) were purchased from the Korea Bank for Pathogenic Viruses (KBPV, Republic of Korea). For HCoV-OC43, its propagation and titration were performed as previously described (*62*) with an additional endpoint dilution assay using MRC-5 lung fibroblast cells at 5 days post-infection. HCoV-229E stocks were stored at -80 °C without further propagation, and titers were determined in MRC-5 cells. SARS-CoV-2 (Omicron BA.2 variant) and MERS-CoV (strain KOR/KNIH/2015) stocks were obtained from the Virus Research Resource Center (VRRC) at the Institute for Basic Science. Viral titers were determined in Vero E6 cells by assessing cytopathic effects (CPE) at 3 days post-infection and calculating $TCID_{50}$/ml by the Spearman–Kärber method.

Small molecule inhibitor and cytotoxicity assay

IACS-010759, ADDA 5 hydrochloride, and Eniluracil (MedChemExpress, USA) were dissolved in DMSO following the manufacturer's instructions. The cytotoxicity of each inhibitor was evaluated in A549-ACE2 or Vero E6 cells using the CellTiter-Glo Luminescent Cell Viability Assay (Promega, USA). For HBE organoids, inhibitors were added to the basolateral side and replenished daily. Organoid viability was measured after 72 h of treatment using the CellTiter-Glo 3D Cell Viability Assay (Promega, USA) following the provided

manual. Luminescence signals were recorded with a multimode microplate reader. Changes in cell viability upon ADDA 5 treatment in HCoV-OC43-infected cells were assessed using the Sulforhodamine B (SRB) assay, as previously described (*63*).

Generation of shRNA-mediated knockdown cells

shRNA oligos targeting *ALAD* and *SLC25A38* were designed from the GPP web portal (Broad Institute) with the highest adjusted score. The hairpin sequences for each target are listed in Table S5A. For shRNA subcloning, the pLKO.1-TRC cloning vector (Addgene, USA) plasmid served as the template. The vector was digested using the restriction enzymes AgeI-HF and EcoRI-HF (New England Biolabs, USA). The digested vector was separated by gel electrophoresis, followed by gel extraction using the Expin Gel SV kit (GeneAll, Republic of Korea). The shRNA oligomers were annealed at 95 °C for 1 min and subsequently ligated together with the digested vector and T4 DNA ligase (New England Biolabs, USA). Ligated plasmids were transformed into DH5α chemically competent *E. coli* (Enzynomics, Republic of Korea) through heat shock transformation. After two days of ampicillin selection, the shRNA plasmid vectors were purified using the NucleoBond Xtra-Midi kit (Macherey-Nagel, Germany). All shRNA subcloning results were validated by difficult Sanger sequencing (Macrogen, Republic of Korea). For the control group, the pLKO.1-scramble shRNA (Addgene, USA) plasmid was processed in the same manner to construct the shScramble plasmid vector.

shRNA-containing lentiviral vectors (LVVs) for control (scramble) and silencing *ALAD* and *SLC25A38* genes were generated following a previously published protocol (*64*). LVVs were then stored at -80 °C and not subjected to multiple freeze-thaw cycles to prevent titer reduction. To knock down target genes, 2.0×10^5 cells were reverse transduced with 100 µl LVVs and 10 ng/ml polybrene in 12-well plates. This was followed by 5 days of puromycin selection to establish the knockdown cells.

Validation of antiviral targets in cell lines

For HCoV-229E, 2.0×10^5 knockdown cells (after shScramble, shALAD, and shSLC25A38 transduction) were plated in a 12-well plate without puromycin. After one day recovery period, cells were infected at the multiplicity of infection (MOI) of 0.01 for 1.5 h at 35°C, followed by a DPBS wash to remove the remaining virus. At 24 hpi, supernatant and cell lysate were collected. The parallel experiment was repeated with MRC-5 WT cells.

For HCoV-OC43, 4.0×10^5 A549-ACE2 cells were seeded in a 6-well plate and maintained at 37 °C with 5% CO_2 for 24 h. Cells were infected with the virus at MOI of 1 for 1 h at 35°C. Following infection, cells were rinsed again and replenished with DMEM (Welgene, Republic of Korea) supplemented with 5% FBS (Gibco, USA), and either DMSO or 20 µM ADDA 5 inhibitor. To assess the impact of the ADDA 5 inhibitor on viral gene expression, total RNA was extracted from cell lysates, and supernatants were collected at 48 hpi.

For SARS-CoV-2 and MERS-CoV, dose-response experiments were carried out using 8.0×10^4 A549-ACE2 or 5.0×10^4 Vero E6 cells seeded in 24-well plates. In the BSL-3 facility, cells were infected at MOI of 0.01 for 1 h at 37°C, washed with DPBS, and then incubated either in growth medium with DMSO or Eniluracil at concentrations ranging from 10 to 100 µM. At 48 hpi, supernatant was harvested for viral RNA quantification and titration.

Validation of antiviral targets in HBE organoids

HBE cells (ScienCell, USA) were expanded in PneumaCult-Ex Plus medium (STEMCELL Technologies, Canada) in a 150 mm cell culture dish. For organoid differentiation under ALI conditions, 8.5×10^4 cells were seeded onto 12-well Transwell plates (Corning, USA). After 2 or 3 days, the apical medium was removed (air-lifted) and the basal

medium was replaced with PneumaCult-ALI medium (STEMCELL Technologies, Canada). Cells were maintained under ALI conditions for 4 weeks to induce differentiation.

Differentiated HBE organoids were pre-rinsed with DPBS and exposed to viral inoculum for 2 h at 37°C. After infection, the inoculum was removed, and the apical side was washed twice with DPBS. For HCoV-OC43, either DMSO or IACS-010759 (10 or 100 nM) was supplied daily to the basal chamber medium. For SARS-CoV-2 and MERS-CoV, DMSO or 100 μM Eniluracil was replenished daily to the basal chamber, together with an additional 10 μL solution applied directly to the apical surface by pipetting. Supernatant was collected at 72 hpi for viral RNA quantification and titration. The remaining organoids were treated with TRIzol (for HCoV-OC43) or fixed with 4% paraformaldehyde (for SARS-CoV-2 and MERS-CoV) for further analyses.

RNA extraction and reverse transcription-quantitative PCR

Total RNA was extracted using TRIzol (Invitrogen, USA) and precipitated with sodium acetate (Invitrogen, USA) and 2-propanol (Sigma-Aldrich, USA). The isolated RNA was treated with DNase I (Takara, Japan), and phase separation was induced using acid-phenol:chloroform, pH 4.5 (Thermo Fisher Scientific, USA). For cDNA synthesis, purified RNA was reverse transcribed using RevertAid reverse transcriptase (Thermo Fisher Scientific, USA). The resulting cDNA was then amplified using RealFast SYBR Kit (Geneer, Republic of Korea), and RT-qPCR was conducted with the QuantStudio 1 Real-Time PCR system (Applied Biosystems, USA). Primers used in this study are listed in Table S5B.

Immunohistochemistry

Immunohistochemical staining of paraffin-embedded HBE organoids was conducted on a BOND RX instrument (Leica, Germany) according to the manufacturer's protocols. Sections were incubated for 60 min at room temperature with either an anti-SARS-CoV-2 nucleocapsid antibody (Abcam, Cat # ab271180) or an anti-MERS-CoV nucleocapsid antibody (SinoBiological, Cat # 400680-MM10). Detection and visualization of viral nucleocapsid protein (NP) were performed using the Bond Polymer Refine Detection kit (Leica, Cat # DS9800), which includes the secondary antibody, hematoxylin counterstain, and DAB (3,3'-diaminobenzidine) chromogen. Viral NP-positive organoids were quantified using QuPath (v0.5.1).

Statistical analysis

Statistical analyses were conducted using GraphPad Prism (version 10.2.2). Statistical details of experiments and analyses are described in the figure legends. Error bars represent the standard error of the mean. A p-value < 0.05 was considered statistically significant (* $p < 0.05$; ** $p < 0.01$; *** $p < 0.001$; **** $p < 0.0001$; n.s., not significant).

ACKNOWLEDGMENTS

We thank all members of the Center for Study of Emerging and Re-emerging Viruses for their helpful discussions and feedback on this paper. We also thank all members of the Hyun Uk Kim and Yoosik Kim laboratories.

Funding

This work was supported by the Institute for Basic Science (IBS-R801-D1 awarded to Y.K.C.), and an internal fund/grant of Electronics and Telecommunications Research Institute (ETRI) (22RB1100, Exploratory and Strategic Research of ETRI-KAIST ICT Future Technology) and the Bio & Medical Technology Development Program of the National Research Foundation (NRF) funded by the Korean government (MSIT) (RS-2024-00509338 and RS-2024-00400771).

Author Contributions

Conceptualization: Young Ki Choi, Hyun Uk Kim, Yoosik Kim
Data curation: Yong-ki Lee, Seongmo Kang, JinA Lim, Kanghee Kim, Se-Mi Kim, Mark Anthony B. Casel, Issac Choi
Formal analysis: Yong-ki Lee, JinA Lim, Se-Mi Kim
Funding acquisition: Young Ki Choi, Hyun Uk Kim, Yoosik Kim
Investigation: Yong-ki Lee, Seongmo Kang, JinA Lim, Kanghee Kim, Se-Mi Kim, Mark Anthony B. Casel, Issac Choi
Methodology: Yong-ki Lee, Seongmo Kang, Kanghee Kim, Se-Mi Kim, Young Ki Choi
Project administration: Young Ki Choi, Hyun Uk Kim, Yoosik Kim
Resources: Yong-ki Lee, Seongmo Kang, Se-Mi Kim, Issac Choi
Software: Yong-ki Lee, Seongmo Kang, Hyun Uk Kim
Visualization: Yong-ki Lee, Seongmo Kang, JinA Lim, Issac Choi
Writing - original draft: Yong-ki Lee, Seongmo Kang, JinA Lim, Kanghee Kim, Young Ki Choi
Writing - review and editing: Young Ki Choi, Hyun Uk Kim, Yoosik Kim

Competing interests

The authors declare that they have no competing interests.

Data and materials availability

All data needed to evaluate the conclusions in the paper are present in the paper or the Supplementary Materials. Any additional information required to reanalyze the data reported in this paper is available from the corresponding author upon request.

REFERENCES

1. K. A. Mayer, J. Stöckl, G. J. Zlabinger, G. A. Gualdoni, Hijacking the Supplies: Metabolism as a Novel Facet of Virus-Host Interaction. *Frontiers in Immunology* **10**, (2019).
2. C. S. Palmer, Innate metabolic responses against viral infections. *Nature Metabolism* **4**, 1245-1259 (2022).
3. J. Thyrsted, C. K. Holm, Virus-induced metabolic reprogramming and innate sensing hereof by the infected host. *Current Opinion in Biotechnology* **68**, 44-50 (2021).
4. K. Girdhar *et al.*, Viruses and Metabolism: The Effects of Viral Infections and Viral Insulins on Host Metabolism. *Annual Review of Virology* **8**, 373-391 (2021).
5. P. Chen, M. Wu, Y. He, B. Jiang, M.-L. He, Metabolic alterations upon SARS-CoV-2 infection and potential therapeutic targets against coronavirus infection. *Signal Transduction and Targeted Therapy* **8**, 237 (2023).
6. S. R. DeVito, E. Ortiz-Riaño, L. Martínez-Sobrido, J. Munger, Cytomegalovirus-mediated activation of pyrimidine biosynthesis drives UDP–sugar synthesis to support viral protein glycosylation. *Proceedings of the National Academy of Sciences* **111**, 18019-18024 (2014).
7. D. C. Schultz *et al.*, Pyrimidine inhibitors synergize with nucleoside analogues to block SARS-CoV-2. *Nature*, (2022).
8. K. S. Greene *et al.*, Glutamine metabolism is essential for coronavirus replication in host cells and in mice. *Journal of Biological Chemistry* **301**, 108063 (2025).
9. S. Yuan *et al.*, SREBP-dependent lipidomic reprogramming as a broad-spectrum antiviral target. *Nat Commun* **10**, 120 (2019).
10. N. Jiménez de Oya *et al.*, Targeting host metabolism by inhibition of acetyl-Coenzyme A carboxylase reduces flavivirus infection in mouse models. *Emerging Microbes & Infections* **8**, 624-636 (2019).
11. J. Chu *et al.*, Pharmacological inhibition of fatty acid synthesis blocks SARS-CoV-2 replication. *Nature Metabolism* **3**, 1466-1475 (2021).
12. R. Narayan *et al.*, Picolinic acid is a broad-spectrum inhibitor of enveloped virus entry that restricts SARS-CoV-2 and influenza A virus in vivo. *Cell Reports Medicine* **4**, 101127 (2023).
13. X. Zheng *et al.*, Taurolithocholic acid protects against viral haemorrhagic fever via inhibition of ferroptosis. *Nature Microbiology* **9**, 2583-2599 (2024).
14. W. D. Jang, S. Jeon, S. Kim, S. Y. Lee, Drugs repurposed for COVID-19 by virtual screening of 6,218 drugs and cell-based assay. *Proceedings of the National Academy of Sciences* **118**, e2024302118 (2021).
15. A. Luttens *et al.*, Ultralarge Virtual Screening Identifies SARS-CoV-2 Main Protease Inhibitors with Broad-Spectrum Activity against Coronaviruses. *J Am Chem Soc* **144**, 2905-2920 (2022).
16. C. Gu, G. B. Kim, W. J. Kim, H. U. Kim, S. Y. Lee, Current status and applications of genome-scale metabolic models. *Genome Biol* **20**, 121 (2019).
17. I. Thiele *et al.*, Personalized whole-body models integrate metabolism, physiology, and the gut microbiome. *Molecular Systems Biology* **16**, e8982 (2020).
18. J. S. Cho, C. Gu, T. H. Han, J. Y. Ryu, S. Y. Lee, Reconstruction of context-specific genome-scale metabolic models using multiomics data to study metabolic rewiring. *Current Opinion in Systems Biology* **15**, 1-11 (2019).
19. A. Ebrahim, J. A. Lerman, B. O. Palsson, D. R. Hyduke, COBRApy: COnstraints-Based Reconstruction and Analysis for Python. *BMC Systems Biology* **7**, 74 (2013).
20. J. E. Lewis, T. E. Forshaw, D. A. Boothman, C. M. Furdui, M. L. Kemp, Personalized Genome-Scale Metabolic Models Identify Targets of Redox Metabolism in Radiation-Resistant Tumors. *Cell Systems* **12**, 68-81.e11 (2021).
21. C. Foguet *et al.*, Genetically personalised organ-specific metabolic models in health and disease. *Nat Commun* **13**, 7356 (2022).

22. A. Heinken *et al.*, A genome-scale metabolic reconstruction resource of 247,092 diverse human microbes spanning multiple continents, age groups, and body sites. *Cell Systems* **16**, (2025).
23. K. Cheng *et al.*, Genome-scale metabolic modeling reveals SARS-CoV-2-induced metabolic changes and antiviral targets. *Molecular Systems Biology* **17**, e10260 (2021).
24. A. T. Ambikan *et al.*, Genome-scale metabolic models for natural and long-term drug-induced viral control in HIV infection. *Life Science Alliance* **5**, e202201405 (2022).
25. K.-L. Chen, F.-S. Wang, Cell-specific genome-scale metabolic modeling of SARS-CoV-2-infected lung to identify antiviral enzymes. *FEBS Open Bio* **13**, 2172-2186 (2023).
26. M. Sertbas, K. O. Ulgen, Uncovering the Effect of SARS-CoV-2 on Liver Metabolism via Genome-Scale Metabolic Modeling for Reprogramming and Therapeutic Strategies. *ACS Omega* **9**, 15535-15546 (2024).
27. A. Renz *et al.*, Metabolic modeling elucidates phenformin and atpenin A5 as broad-spectrum antiviral drugs against RNA viruses. *Communications Biology* **8**, 791 (2025).
28. J. L. Robinson *et al.*, An atlas of human metabolism. *Sci Signal* **13**, eaaz1482 (2020).
29. J. Lim *et al.*, Genome-scale knockout simulation and clustering analysis of drug-resistant breast cancer cells reveal drug sensitization targets. *Proceedings of the National Academy of Sciences* **122**, e2425384122 (2025).
30. E. R. S. Kunji, M. S. King, J. J. Ruprecht, C. Thangaratnarajah, The SLC25 Carrier Family: Important Transport Proteins in Mitochondrial Physiology and Pathology. *Physiology* **35**, 302-327 (2020).
31. C. R. Oliva *et al.*, Identification of Small Molecule Inhibitors of Human Cytochrome c Oxidase That Target Chemoresistant Glioma Cells. *Journal of Biological Chemistry* **291**, 24188-24199 (2016).
32. C. R. Oliva, W. Zhang, C. Langford, M. J. Suto, C. E. Griguer, Repositioning chlorpromazine for treating chemoresistant glioma through the inhibition of cytochrome c oxidase bearing the COX4-1 regulatory subunit. *Oncotarget* **8**, (2017).
33. A. H. d. Wilde *et al.*, Screening of an FDA-Approved Compound Library Identifies Four Small-Molecule Inhibitors of Middle East Respiratory Syndrome Coronavirus Replication in Cell Culture. *Antimicrobial Agents and Chemotherapy* **58**, 4875-4884 (2014).
34. M. Plaze *et al.*, Inhibition of the replication of SARS-CoV-2 in human cells by the FDA-approved drug chlorpromazine. *International Journal of Antimicrobial Agents* **57**, 106274 (2021).
35. J. Dyall *et al.*, Repurposing of Clinically Developed Drugs for Treatment of Middle East Respiratory Syndrome Coronavirus Infection. *Antimicrobial Agents and Chemotherapy* **58**, 4885-4893 (2014).
36. H. Kim *et al.*, Diverse bat organoids provide pathophysiological models for zoonotic viruses. *Science* **388**, 756-762 (2025).
37. L. Lin *et al.*, Human airway submucosal gland organoids to study respiratory inflammation and infection. *Cell Stem Cell* **32**, 1170-1182.e1177 (2025).
38. W. Lee *et al.*, A single-cell atlas of in vitro multiculture systems uncovers the in vivo lineage trajectory and cell state in the human lung. *Experimental & Molecular Medicine* **55**, 1831-1842 (2023).
39. D. Park *et al.*, Differential beta-coronavirus infection dynamics in human bronchial epithelial organoids. *Journal of Medical Virology* **96**, e29600 (2024).
40. J. Gustafsson *et al.*, DSAVE: Detection of misclassified cells in single-cell RNA-Seq data. *Plos One* **15**, e0243360 (2020).
41. I. Halabitska *et al.*, Metformin in Antiviral Therapy: Evidence and Perspectives. *Viruses* **16**, 1938 (2024).
42. D. Movia, D. Bazou, Y. Volkov, A. Prina-Mello, Multilayered Cultures of NSCLC cells grown at the Air-Liquid Interface allow the efficacy testing of inhaled anti-cancer drugs. *Sci Rep-Uk* **8**, 12920 (2018).
43. Yoav D. Shaul *et al.*, Dihydropyrimidine Accumulation Is Required for the Epithelial-Mesenchymal Transition. *Cell* **158**, 1094-1109 (2014).

44. S. A. H. van den Wildenberg *et al.*, Quantification of uracil, dihydrouracil, thymine and dihydrothymine for reliable dihydropyrimidine dehydrogenase (DPD) phenotyping critically depend on blood and plasma storage conditions. *Journal of Pharmaceutical and Biomedical Analysis* **221**, 115027 (2022).
45. Q. Xin *et al.*, Metabolomic alterations in the plasma of patients with various clinical manifestations of COVID-19. *Virol J* **21**, 266 (2024).
46. S. Newstead, Future opportunities in solute carrier structural biology. *Nature Structural & Molecular Biology* **31**, 587-590 (2024).
47. A. Khan, Y. Liu, M. Gad, T. C. Kenny, K. Birsoy, Solute carriers: The gatekeepers of metabolism. *Cell* **188**, 869-884 (2025).
48. H. Yan *et al.*, Sodium taurocholate cotransporting polypeptide is a functional receptor for human hepatitis B and D virus. *eLife* **1**, e00049 (2012).
49. J.-H. Park *et al.*, Structural insights into the HBV receptor and bile acid transporter NTCP. *Nature* **606**, 1027-1031 (2022).
50. N. N. T. Nguyen *et al.*, Hepatitis C Virus Modulates Solute carrier family 3 member 2 for Viral Propagation. *Sci Rep-Uk* **8**, 15486 (2018).
51. L. He *et al.*, The Solute Carrier Transporter SLC15A3 Participates in Antiviral Innate Immune Responses against Herpes Simplex Virus-1. *Journal of Immunology Research* **2018**, 5214187 (2018).
52. A. Moskovskich *et al.*, The transporters SLC35A1 and SLC30A1 play opposite roles in cell survival upon VSV virus infection. *Sci Rep-Uk* **9**, 10471 (2019).
53. J. Y. Ryu, H. U. Kim, S. Y. Lee, Framework and resource for more than 11,000 gene-transcript-protein-reaction associations in human metabolism. *Proceedings of the National Academy of Sciences* **114**, E9740-E9749 (2017).
54. H. U. Kim, T. Y. Kim, S. Y. Lee, Framework for network modularization and Bayesian network analysis to investigate the perturbed metabolic network. *BMC Systems Biology* **5**, S14 (2011).
55. D. Segrè, D. Vitkup, G. M. Church, Analysis of optimality in natural and perturbed metabolic networks. *Proceedings of the National Academy of Sciences* **99**, 15112-15117 (2002).
56. L. McInnes, J. Healy, UMAP: Uniform Manifold Approximation and Projection for Dimension Reduction. *ArXiv* **abs/1802.03426**, (2018).
57. P. W. Harrison *et al.*, Ensembl 2024. *Nucleic Acids Research* **52**, D891-D899 (2023).
58. L. Wang, Z. Feng, X. Wang, X. Wang, X. Zhang, DEGseq: an R package for identifying differentially expressed genes from RNA-seq data. *Bioinformatics* **26**, 136-138 (2009).
59. M. I. Love, W. Huber, S. Anders, Moderated estimation of fold change and dispersion for RNA-seq data with DESeq2. *Genome Biol* **15**, 550 (2014).
60. T. Wu *et al.*, clusterProfiler 4.0: A universal enrichment tool for interpreting omics data. *Innovation (Camb)* **2**, 100141 (2021).
61. Z. Gu, R. Eils, M. Schlesner, Complex heatmaps reveal patterns and correlations in multidimensional genomic data. *Bioinformatics* **32**, 2847-2849 (2016).
62. Y. Song *et al.*, Anti-viral, anti-bacterial, but non-cytotoxic nanocoating for reusable face mask with efficient filtration, breathability, and robustness in humid environment. *Chemical Engineering Journal* **470**, 144224 (2023).
63. S. Tan, S. Kim, Y. Kim, Targeting mitochondrial RNAs enhances the efficacy of the DNA-demethylating agents. *Sci Rep-Uk* **14**, 30767 (2024).
64. N. E. Sanjana, O. Shalem, F. Zhang, Improved vectors and genome-wide libraries for CRISPR screening. *Nature Methods* **11**, 783-784 (2014).

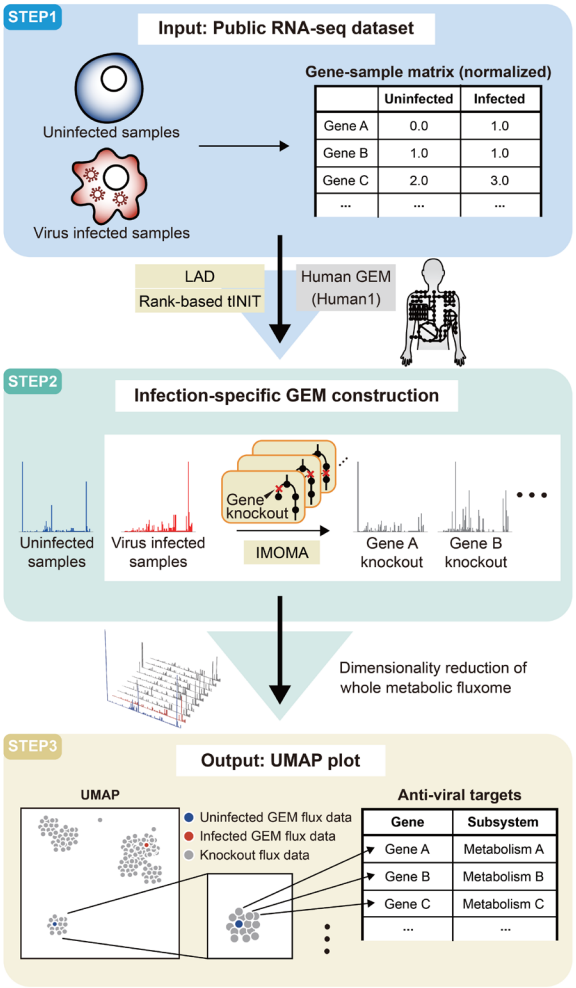

Figure 1. Schematic workflow of establishing the computational framework for antiviral target identification.

A schematic workflow illustrating the framework for identifying antiviral targets using transcriptomics datasets. The framework consists of three key steps. First, a normalized gene-sample matrix derived from an RNA-seq dataset containing both uninfected and virus-infected samples is used as the input. Human-GEM (Human1) serves as the template, and infection-specific GEMs are constructed using the rank-based tINIT. Flux profiles (fluxomes) are inferred by the LAD. Second, single-gene knockout simulations are performed on the virus-infected GEMs to generate additional GEMs for each knockout event. Flux changes after gene knockout are predicted using the lMOMA method. Third, all fluxomes (uninfected, infected, and knockouts) are embedded via UMAP. In the UMAP plot, genes with knockout fluxomes that co-cluster with those of uninfected cells are considered potential antiviral targets.

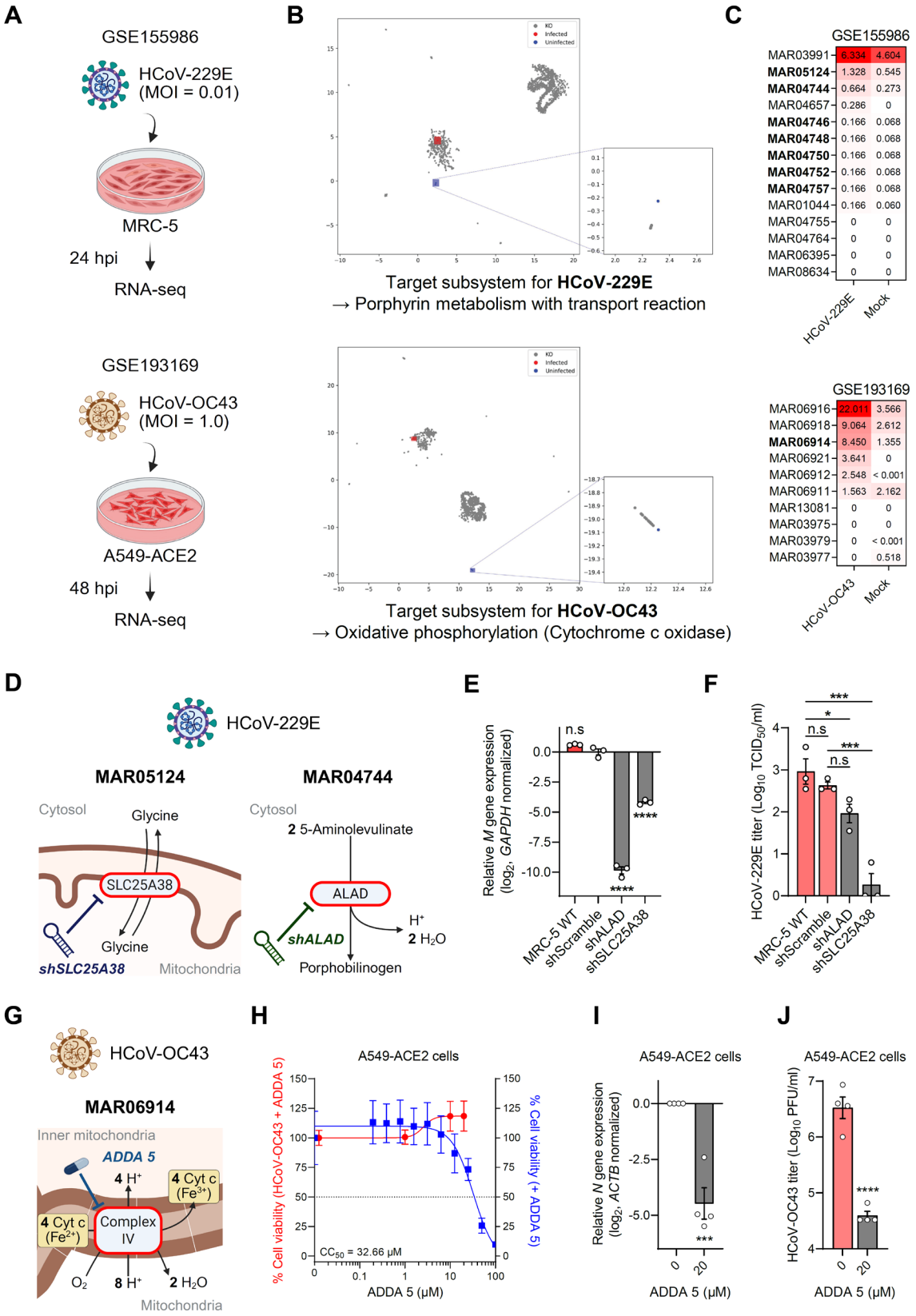
A
GSE155986
HCoV-229E
(MOI = 0.01)
MRC-5
24 hpi
RNA-seq
GSE193169
HCoV-OC43
(MOI = 1.0)
A549-ACE2
48 hpi
RNA-seq
B
KO
Infected
Uninfected
Target subsystem for HCoV-229E
→ Porphyrin metabolism with transport reaction
Target subsystem for HCoV-OC43
→ Oxidative phosphorylation (Cytochrome c oxidase)
C
GSE155986
MAR03991 6.334 4.604
MAR05124 1.328 0.545
MAR04744 0.664 0.273
MAR04657 0.286 0
MAR04746 0.166 0.068
MAR04748 0.166 0.068
MAR04750 0.166 0.068
MAR04752 0.166 0.068
MAR04757 0.166 0.068
MAR01044 0.166 0.060
MAR04755 0 0
MAR04764 0 0
MAR06395 0 0
MAR08634 0 0
HCoV-229E
Mock
GSE193169
MAR06916 22.011 3.566
MAR06918 9.064 2.612
MAR06914 8.450 1.355
MAR06921 3.641 0
MAR06912 2.548 < 0.001
MAR06911 1.563 2.162
MAR13081 0 0
MAR03975 0 0
MAR03979 0 < 0.001
MAR03977 0 0.518
HCoV-OC43
Mock
D
HCoV-229E
MAR05124
MAR04744
Cytosol
Glycine
SLC25A38
Glycine
shSLC25A38
Mitochondria
Cytosol
2 5-Aminolevulinate
ALAD
shALAD
H+
2 H2O
Porphobilinogen
E
n.s
****
****
Relative M gene expression
(log2, GAPDH normalized)
MRC-5 WT
shScramble
shALAD
shSLC25A38
F
***
*
n.s
***
n.s
HCoV-229E titer (Log10 TCID50/ml)
MRC-5 WT
shScramble
shALAD
shSLC25A38
G
HCoV-OC43
MAR06914
Inner mitochondria
ADDA 5
4 H+
4 Cyt c
(Fe3+)
4 Cyt c
(Fe2+)
Complex
IV
O2
8 H+
2 H2O
Mitochondria
H
A549-ACE2 cells
% Cell viability (HCoV-OC43 + ADDA 5)
% Cell viability (+ ADDA 5)
CC50 = 32.66 μM
ADDA 5 (μM)
I
A549-ACE2 cells
Relative N gene expression
(log2, ACTB normalized)
***
ADDA 5 (μM)
J
A549-ACE2 cells
HCoV-OC43 titer (Log10 PFU/ml)
****
ADDA 5 (μM)

Figure 2. Discovery of antiviral targets for HCoV-OC43 and HCoV-229E.

(A) Graphical summary of the experimental design for two public RNA-seq datasets, GSE155986 and GSE193169, used as input data for the computational framework. Images were created with BioRender.com.

(B) UMAP plots showing the fluxome comparisons across all GEMs generated using the GSE155986 or GSE193169 dataset. The uninfected sample is represented in blue, the virus-infected sample in red, and the single-gene knockout simulation results as gray dots. Detailed gene lists are provided in Table S1.

(C) Metabolic flux profiles of the porphyrin subsystem in HCoV-229E-infected samples and the OXPHOS subsystem in HCoV-OC43-infected samples, compared with uninfected controls. Predicted antiviral target reactions are highlighted in bold.

(D) Schematic representation of reactions involving SLC25A38 and ALAD with shRNA-mediated inhibitory strategies (adapted from https://metabolicatlas.org/). Images were created with BioRender.com.

(E) Intracellular HCoV-229E membrane (*M*) gene expression at 24 hpi was quantified via RT-qPCR (n = 3). *GAPDH* was used as the housekeeping gene, and expression was normalized using the $\Delta\Delta C_t$ (-ddC_t) method. Statistical significance was calculated using one-way ANOVA with Dunnett's multiple comparison test.

(F) Extracellular HCoV-229E titers at 24 hpi were measured by the endpoint dilution assay (n = 3). Statistical significance was calculated using one-way ANOVA with Dunnett's multiple comparison test. $TCID_{50}$: tissue culture infectious dose 50%.

(G) Schematic representation of the OXPHOS complex IV (cytochrome c oxidase) reaction and its inhibition by ADDA 5 (adapted from https://metabolicatlas.org/). Images were created with BioRender.com. Cyt c: cytochrome c.

(H) Dose-response curves for ADDA 5 in A549-ACE2 cells, showing uninfected cell viability (blue, n = 4) and viability of HCoV-OC43-infected cells with post-treatment (red, n = 2). Curves were fitted by nonlinear four-parameter sigmoidal regression in GraphPad Prism.

(I) Intracellular HCoV-OC43 nucleocapsid (*N*) gene expression at 48 hpi was quantified via RT-qPCR (n = 4). *ACTB* was used as the housekeeping gene, and expression was normalized using the -ddC_t method. Statistical significance was calculated using a one-tailed Student's t-test.

(J) Extracellular HCoV-OC43 titers at 48 hpi were measured by the plaque assay (n = 4). Statistical significance was calculated using a one-tailed Student's t-test. PFU: plaque-forming unit.

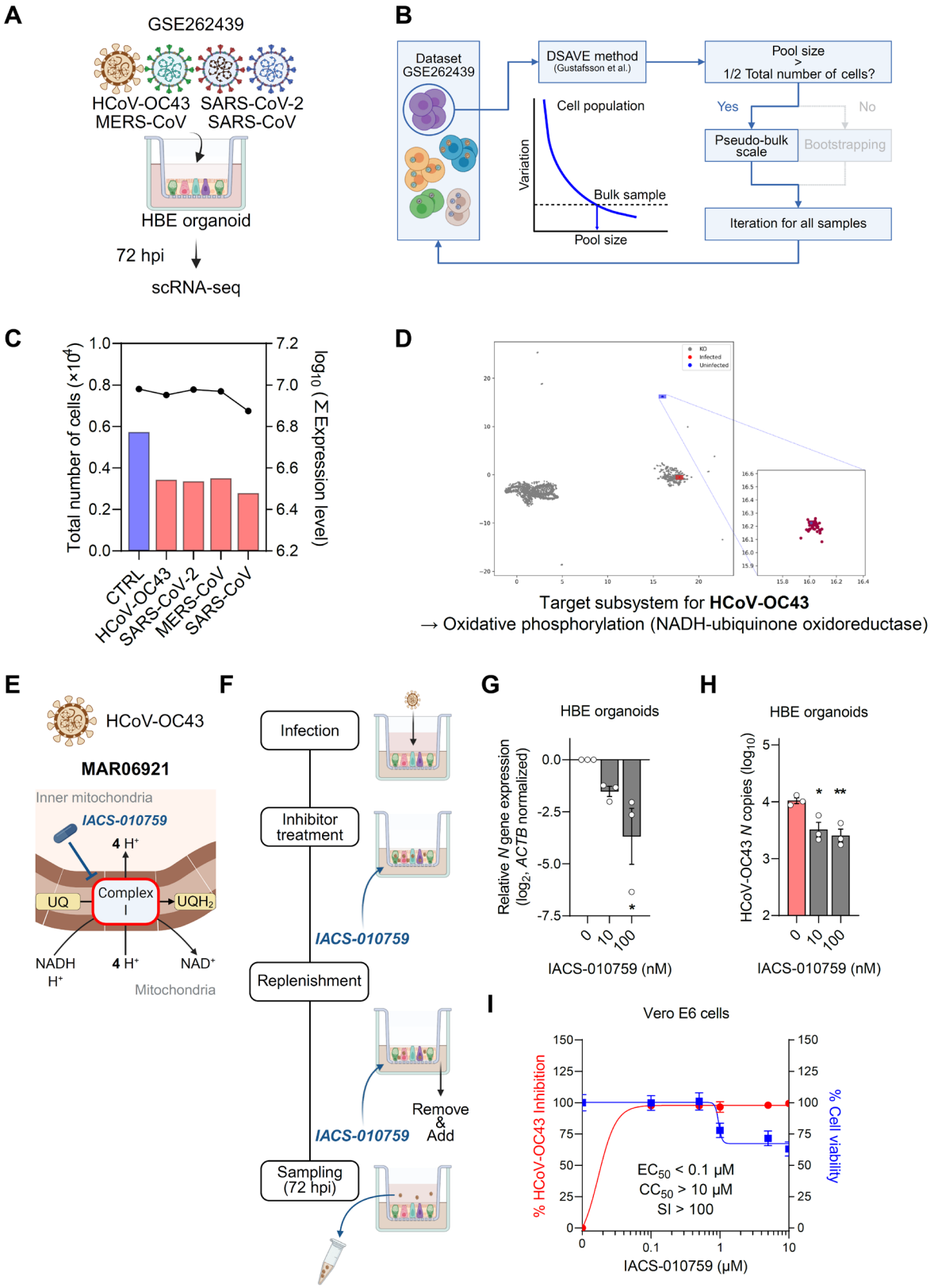
A
GSE262439
HCoV-OC43
MERS-CoV
SARS-CoV-2
SARS-CoV
HBE organoid
72 hpi
scRNA-seq
B
Dataset GSE262439
DSAVE method (Gustafsson et al.)
Pool size > 1/2 Total number of cells?
Yes
No
Pseudo-bulk scale
Bootstrapping
Iteration for all samples
Cell population
Variation
Bulk sample
Pool size
C
Total number of cells (×10⁴)
log10 (Σ Expression level)
CTRL
HCoV-OC43
SARS-CoV-2
MERS-CoV
SARS-CoV
D
Target subsystem for HCoV-OC43
→ Oxidative phosphorylation (NADH-ubiquinone oxidoreductase)
E
HCoV-OC43
MAR06921
Inner mitochondria
IACS-010759
4 H+
UQ
Complex I
UQH2
NADH H+
4 H+
NAD+
Mitochondria
F
Infection
Inhibitor treatment
IACS-010759
Replenishment
Remove & Add
IACS-010759
Sampling (72 hpi)
G
HBE organoids
Relative N gene expression (log2, ACTB normalized)
IACS-010759 (nM)
H
HBE organoids
HCoV-OC43 N copies (log10)
IACS-010759 (nM)
I
Vero E6 cells
% HCoV-OC43 Inhibition
% Cell viability
EC50 < 0.1 μM
CC50 > 10 μM
SI > 100
IACS-010759 (μM)

Figure 3. Application of the framework to HCoV-OC43-infected HBE organoids.
(A) Graphical summary of the experimental design for the previously published scRNA-seq dataset GSE262439. Images were created with BioRender.com.
(B) Schematic flow of applying the DSAVE method. The cell pooling size (a threshold of CPM > 0.5) was estimated based on the total variation score. If the estimated pooling size did not exceed half of the total number of cells in a sample group, bootstrapping with random mixing was performed; otherwise, the entire sample was used at the pseudo-bulk scale. This procedure was repeated for each sample group individually. Images were created with BioRender.com.
(C) Total number of cells (bars) and gene expression levels (points with connecting lines) for each sample group used in constructing infection-specific GEMs. Expression levels represent normalized RNA counts.
(D) UMAP plots comparing fluxomes across all GEMs derived from the GSE262439 dataset for HCoV-OC43. The uninfected sample is represented in blue, the virus-infected sample in red, and the single-gene knockout simulation results as gray dots. A detailed gene list is provided in Table S2.
(E) Schematic representation of the OXPHOS complex I (NADH-ubiquinone oxidoreductase) reaction and its inhibition by IACS-010759 (adapted from https://metabolicatlas.org/). Images were created with BioRender.com. UQ: ubiquinone, UQH_2: ubiquinol.
(F) Experimental design for evaluating the anti-HCoV-OC43 effect of IACS-010759 in HBE organoids (see *Materials and Methods* for details). Images were created with BioRender.com.
(G) Intracellular HCoV-OC43 nucleocapsid (*N*) gene expression at 72 hpi was quantified via RT-qPCR (n = 3). *ACTB* was used as the housekeeping gene, and expression was normalized using the -ddC_t method. Statistical significance was calculated using one-way ANOVA with Dunnett's multiple comparison test.
(H) Extracellular HCoV-OC43 RNA copies at 72 hpi were quantified by RT-qPCR targeting nucleocapsid (*N*) amplicon. For each sample, 100 µl of viral supernatant was collected from infected HBE organoids (n = 3). Statistical significance was calculated using one-way ANOVA with Dunnett's multiple comparison test.
(I) Dose-response analysis for IACS-010759 in Vero E6 cells. Cell viability after 72 h of treatment (blue curve, n = 4) and HCoV-OC43 titer at 72 hpi (red curve, n = 4) were measured. Curves were fitted by nonlinear four-parameter sigmoidal regression in GraphPad Prism. HCoV-OC43 inhibition (%) was calculated relative to DMSO controls. SI: selectivity index.

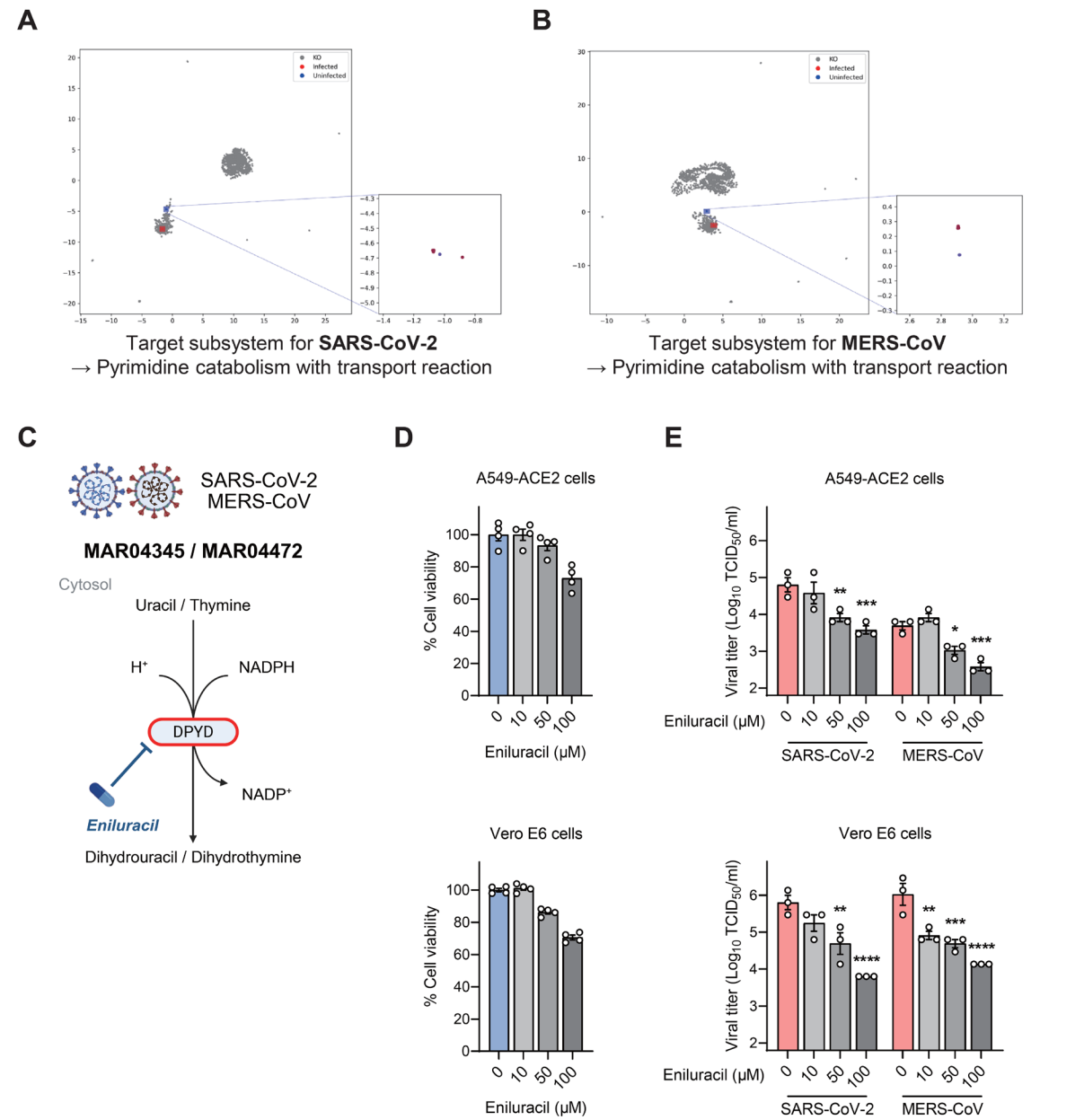

Figure 4. Application of the framework for SARS-CoV-2- and MERS-CoV-infected HBE organoids.

(A and B) UMAP plots comparing fluxomes across all GEMs derived from the GSE262439 dataset for SARS-CoV-2 **(A)** and MERS-CoV **(B)**. The uninfected sample is represented in blue, the virus-infected sample in red, and the single-gene knockout simulation results as gray dots. Detailed gene lists are provided in Table S3.

(C) Schematic representation of the reaction involving DPYD and its inhibition by Eniluracil (adapted from https://metabolicatlas.org/). Images were created with BioRender.com.

(D) Dose-response analysis for Eniluracil in A549-ACE2 and Vero E6 cells. Cell viability was measured after 48 h of treatment (n = 4).

(E) Extracellular SARS-CoV-2 and MERS-CoV titers at 48 hpi were measured by the endpoint dilution assay (n = 3). Statistical significance was calculated using two-way ANOVA with Dunnett's multiple comparison test.

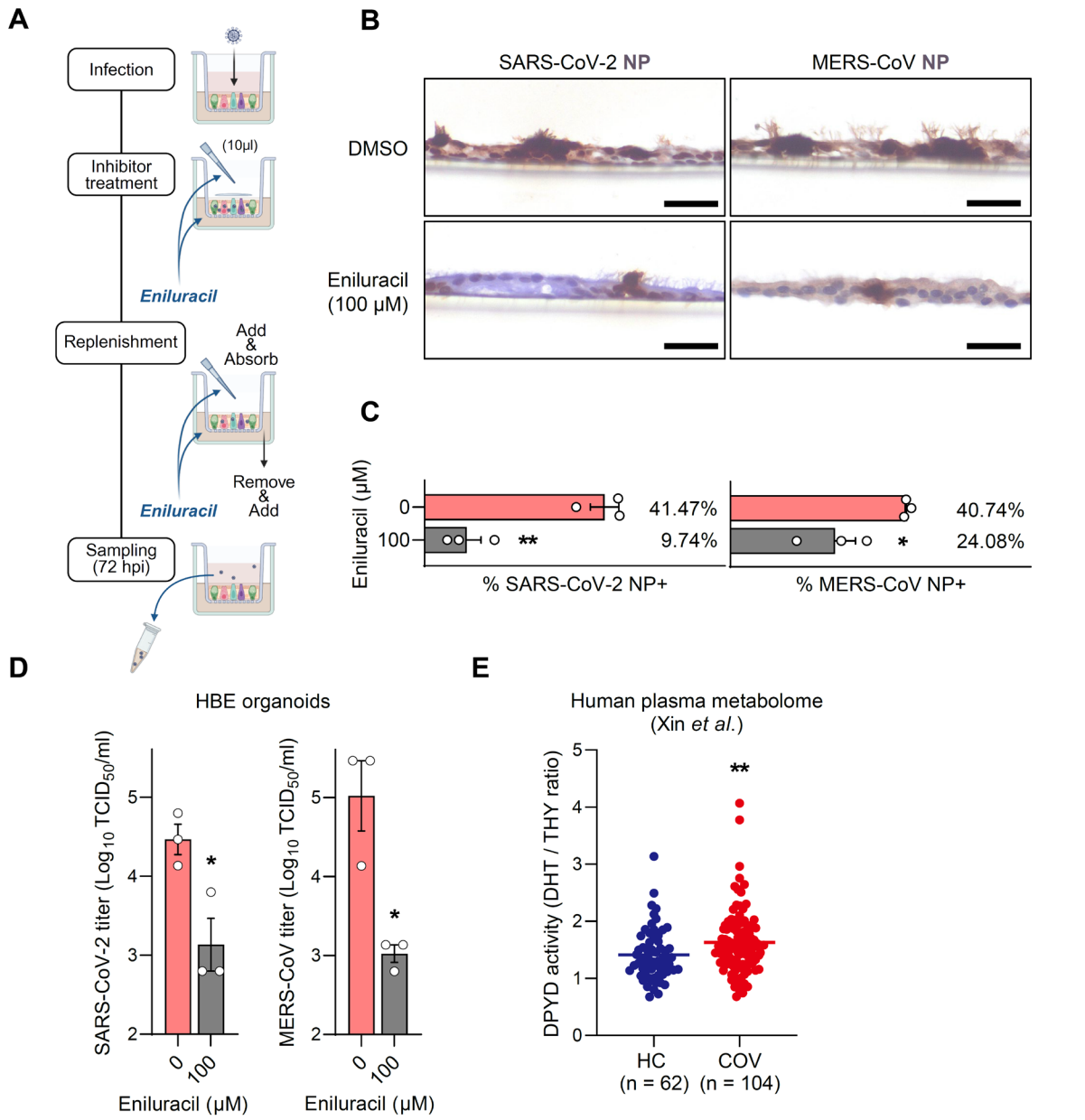

Figure 5. Effects of DPYD inhibition on SARS-CoV-2 and MERS-CoV replication

(A) Experimental design for evaluating the anti-SARS-CoV-2 and -MERS-CoV effects of Eniluracil in HBE organoids (see *Materials and Methods* for details). Images were created with BioRender.com.

(B) Representative IHC images of organoid sections. Viral nucleocapsid (NP) was used as the infection marker for each virus. Scale bar = 20 μm.

(C) Quantification of NP-positive (NP+) organoids (n = 3). The NP+ fraction was calculated as NP+ area divided by total cellular area, with areas measured using QuPath software. Statistical significance was calculated using a one-tailed Student's t-test.

(D) Extracellular SARS-CoV-2 and MERS-CoV titers at 72 hpi were measured by the endpoint dilution assay (n = 3). Statistical significance was calculated using a one-tailed Student's t-test.

(E) Re-analysis of a human plasma metabolome dataset (n = 166). DPYD enzymatic activity was calculated as the ratio of DHT to THY (raw intensities) for each sample (HC: healthy control, COV: COVID-19 patient). Statistical significance was calculated using a two-tailed Welch's t-test.